

Ionic conduction properties of nanocrystalline $\text{Er}_2\text{Ti}_2\text{O}_7$ functional material

K. Sandeep

Department of Physics, Mar Ivanios College, Thiruvananthapuram 695015, Kerala, India

E-mail: sandeepkollam@gmail.com

Abstract. The rare-earth titanate $\text{Er}_2\text{Ti}_2\text{O}_7$ nanoceramic prepared by the modified combustion technique exhibits cubic pyrochlore structure with the space group $Fd\bar{3}m$. Powder XRD and vibrational spectroscopic tools have been used for structural identification and confirmation. The detailed optical and photoluminescence (PL) properties of the sample have been analyzed using UV-Vis diffuse reflectance spectroscopy and PL spectroscopy. Impedance spectroscopic studies have revealed that the material exhibits conduction by hopping of ions, which increases with temperature. Z-View software has been used to fit the impedance data and deduce the electrical parameters of the samples from the equivalent circuit. The grain activation energy is less than that of grain boundary, which implies that grain conduction is predominant in the sample. The optical and electrical studies confirm that the material is a possible candidate to fabricate optical devices and construct solid oxide fuel cells.

Keywords: nanostructures, pyrochlore, optical properties, ionic conduction, impedance spectroscopy.

<https://doi.org/10.15407/spqeo23.01.52>

PACS 62.23.St, 66.30.Dn, 78.67.-n, 84.37.+a

Manuscript received 20.07.19; revised version received 26.12.19; accepted for publication 18.03.20; published online 23.03.20.

1. Introduction

The pyrochlore oxides with the general formula $\text{A}_2\text{B}_2\text{O}_7$ has achieved a remarkable place in the materials research industry due to their various properties that can be tailored to generate material with desired properties. These materials find applications in many fields such as optical, nuclear waste removal, catalysts and semiconductor industries [1-4]. They can be also used as photocatalysts, thermal barrier coatings and solid oxide fuel cells (SOFC) due to moderate ionic conductivity [5-7]. The titanium-based pyrochlore oxides have brought up many applications in the areas of technological interests depending on the chemical elements involved [8-12]. It is also possible to develop solar cells and microelectronic devices using titanium-based materials [13]. The insulating pyrochlore rare-earth oxides ($\text{A}_2\text{B}_2\text{O}_7$) have the face-centered cubic crystal structure with the space group $Fd\bar{3}m$, where A is the larger transition metal and B^{4+} ions are smaller one, situated at the sublattices of corner-sharing tetrahedra and occupy the sites 16d and 16c, respectively, having the D_{3d} symmetry [14]. Many rare-earth metal oxides are known for their special photoluminescence properties

that can be used for display applications. These nanoscale phosphor materials have good luminescence characteristics, stability in high vacuum, and absence of corrosive gas emission under electron bombardment [15]. Spin Teller effect leads to lattice distortion but no spin order is noticed in $\text{Er}_2\text{Ti}_2\text{O}_7$ prepared by conventional solid-state reaction [16].

This paper reports the structural, vibrational, optical and electrical characterizations of rare-earth titanate $\text{Er}_2\text{Ti}_2\text{O}_7$ nanomaterial prepared by the modified combustion technique for the first time.

2. Experimental

The rare-earth titanate $\text{Er}_2\text{Ti}_2\text{O}_7$ nanoceramic (hereafter abbreviated as ETO) was prepared through the modified combustion technique [17, 18]. Stoichiometric amounts of the starting materials were weighed and dissolved in suitable solvents. Citric acid ($\text{C}_6\text{H}_8\text{O}_7 \cdot \text{H}_2\text{O}$) was used as a complexing agent and aqueous ammonia – as a fuel reagent. Er_2O_3 was dissolved in concentrated nitric acid and $\text{ZrOCl}_2 \cdot 8\text{H}_2\text{O}$ in double distilled water and titanium isopropoxide ($\text{C}_{12}\text{H}_{28}\text{O}_4\text{Ti}$) in methanol. These solutions in a glass beaker were mixed well by using a magnetic

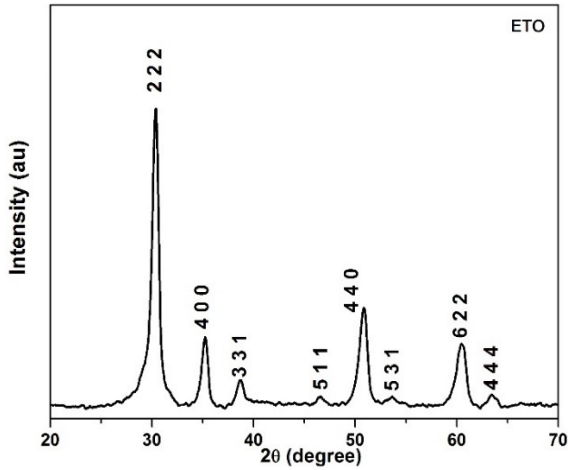


Fig. 1.

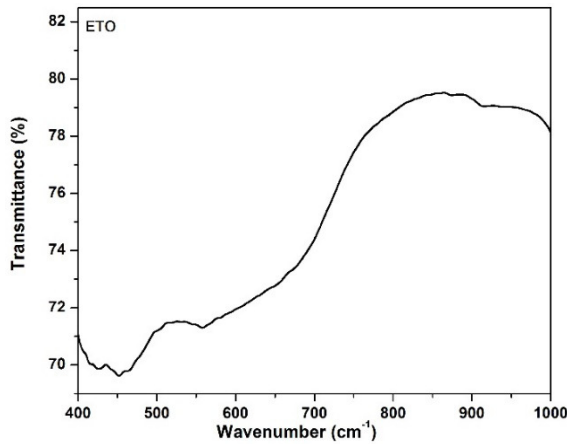


Fig. 2.

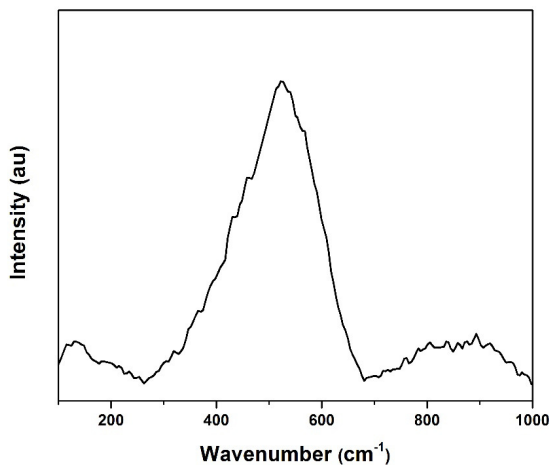


Fig. 3.

stirrer. pH of the solution was adjusted to a value just above 7 to get a successful combustion. The clear solution was heated using a hot plate at 250 °C in a ventilated fume hood. The solution boiled and on persistent heating got auto-ignited to produce combustion product. This

powder was annealed for 2 hours in an oxygen atmosphere at 600 °C to eliminate the presence of organic impurities generated due to combustion.

The XRD patterns of the materials were recorded at room temperature using a Bruker D8 X-ray powder diffractometer with $\text{CuK}\alpha$ radiation of the wavelength 1.5405 Å in a widerange of Bragg angle with a step size of 0.02. Raman spectra were measured using an alpha 300 RA spectrometer with 532 nm DPSS laser with the power 70 mW. The Fourier transform infrared (FT-IR) spectra of the compounds were tested with the spectrum 2 Perkin–Elmer Fourier transform infrared spectrometer by using KBr pellets. The UV-Vis diffuse reflectance spectra were recorded with the Perkin–Elmer Lambda 35 UV-Vis spectrophotometer by using an integrated sphere accessory (Labsphere RSA-PE-20). The photoluminescence spectra were obtained using the JASCO FP-8500 spectrofluorometer with SCE-846 accessory. The impedance and related parameters were measured using the computer controlled LCR meter Hioki Hi Tester 3532 50, as a function of temperature over a wide range of frequencies (100 Hz...5 MHz) and temperatures (350 °C...850 °C). The sample powders were mixed with 1 wt.% solution of binder polyvinyl alcohol and uniaxially pressed in a hydraulic press at the pressure close to 190 MPa to produce cylindrical pellet with the thickness 2 mm and 12 mm in diameter. The pellet made from the sample ETO was heated up to 1400 °C and obtained a density of more than 97% of the theoretical one. The density values of the pellet were determined using Archimedes principle. Conducting silver paste contacts were applied to two parallel surfaces of the pellet and preheated at 900 °C for 1 h for impedance measurements.

3. Results and discussion

The powder XRD pattern of ETO nanoceramic has been shown in Fig. 1. This pattern can be well indexed with ICDD file No. 73-1647, which gives the structure of an ideal cubic pyrochlore belonging to $Fd\bar{3}m$ [227] space group with $Z = 8$. The powder XRD pattern of the sample ETO is comparable to earlier reports for $\text{Er}_2\text{Ti}_2\text{O}_7$ [16]. The crystallite size was determined from the broadening of corresponding X-ray spectral peaks by using the Scherrer formula. The average crystallite size is found as 13.90 nm and the unit cell parameter is 10.1371. The line broadening in the XRD pattern indicates the nanonature of the material.

Fourier transform infrared spectroscopy is extensively used for studying the nature of metal-oxygen bonds in the pyrochlore oxides. The infrared active optic modes in pyrochlores are generated from the bending and stretching vibrations of the metal–oxygen bonds. The infrared lattice vibration frequencies of the pyrochlore compounds with the general formula $\text{A}_2\text{B}_2\text{O}_7$ gives seven IR-active optic modes from a group theoretical analysis [19]. FT-IR transmittance spectrum of the nanopowder samples over the range 400 to 1000 cm^{-1} is given in Fig. 2. In this study, a total of three characteristic IR

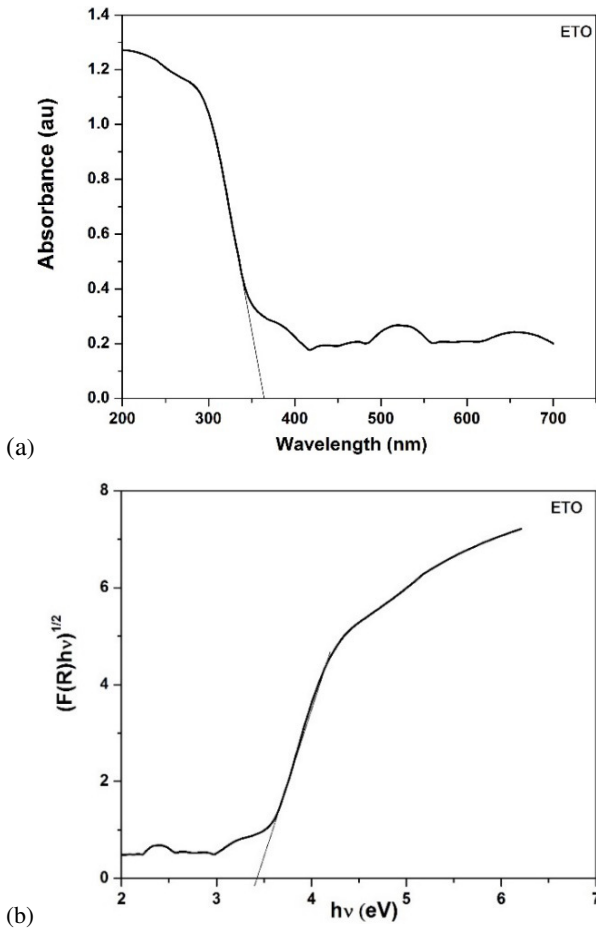


Fig. 4.

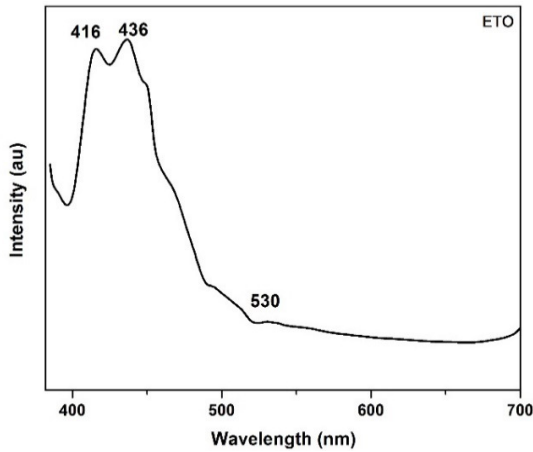


Fig. 5.

absorption bands are identified. The strong band observed at 455 cm^{-1} is originated from the stretching of RE-O' and is assigned to F_{1u} . The medium absorption band at 561 cm^{-1} and the broad absorption band shown as a shoulder at 694 cm^{-1} are related with the Ti-O stretching vibration in TiO_6 octahedron and are assigned to F_{1u} band. The band at 561 cm^{-1} with the shoulder

694 cm^{-1} occurs as the characteristic absorption bands in the titanium pyrochlore spectra [19, 20]. The above absorption bands give the evidence that the prepared sample is of pyrochlore structure.

Raman spectroscopy is more surface oriented than XRD because an excitation energy in the near IR region is less penetrating than X-rays. A comparison of Raman spectroscopy with XRD can be used to study the difference between the surface and bulk configurations of pyrochlore powders [21]. The obtained Raman spectrum of ETO is shown in Fig. 3. The bands in the Raman spectra are tentatively assigned to symmetry species by comparing with previously published Raman spectra of pyrochlore oxides. The weak band at 124 cm^{-1} is present due to the vibration of the crystal lattice. The strong band at 524 cm^{-1} is assigned to A_{1g} mode, which is attributed to RE-O stretching [20, 22, 23]. The weak band at 870 cm^{-1} is generated due to the second-order Raman scattering [24]. Both Raman and FT-IR vibrational spectroscopic studies agree well with the XRD analysis.

UV-visible diffuse reflectance spectroscopy is a useful spectroscopic technique that probes into the electronic structure and domain size of transition-metal oxides. The UV-Vis optical absorption spectra of the sample ETO recorded in the diffuse reflectance mode in the range 200 to 700 nm are given in Fig. 4a. It is observed that ETO exhibits an almost similar absorbance in the broad UV-visible region with absorption edges at 365 nm, which is assigned to the intrinsic bandgap absorption of the sample.

Determination of the optical band gap was performed using the Tauc equation, which gave the dependence on the photon energy in the high energy absorption region [25]. According to this relation, the band gap (E_g) of material is as follows:

$$\alpha h\nu = B(h\nu - E_g)^m, \quad (1)$$

$$F(R) = \frac{(1-R)^2}{2R}, \quad (2)$$

where the absorption coefficient (α) is proportional to $F(R)$ the Kubelka-Munk function, R represents the reflectance (%), h is the Planck constant, ν represents the frequency of the incident photon, B is the energy independent constant, and m is an index representing the nature of electronic transition. The value of $m = 2$ for an indirect allowed transition, $m = 3$ for an indirect forbidden transition, $m = 1/2$ for a direct allowed transition, $m = 3/2$ for a direct forbidden transition [26-28]. E_g values were obtained by extrapolating the slope, to $(\alpha h\nu)^{1/2} = 0$, in the Tauc plot given in Fig. 4b. Thus, the band gap energy value obtained for ETO is 3.39 eV. This value is comparable to E_g value deduced from the absorption spectra [29].

Table 1. Transitions corresponding to different wavelengths of ETO.

Compound	Excitation wavelength (nm)	Emission wavelength (nm)	Element	Lower-upper transition
ETO	365	416	Ti	${}^5F_2 - {}^3D_0$
		436	Er	${}^3H_5 - {}^0A_6$
		530	Er	${}^3H_5 - {}^0A_5$

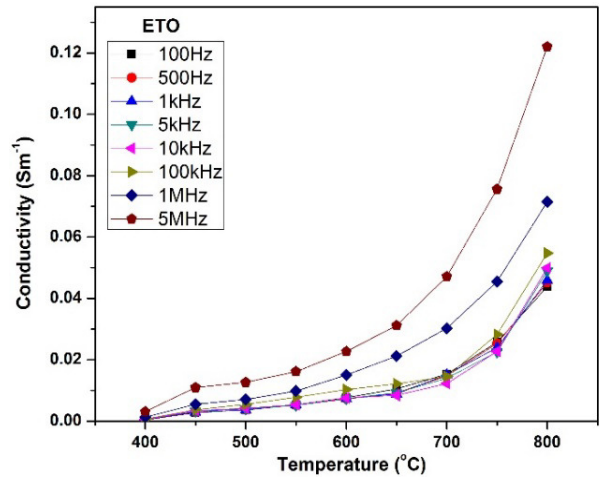
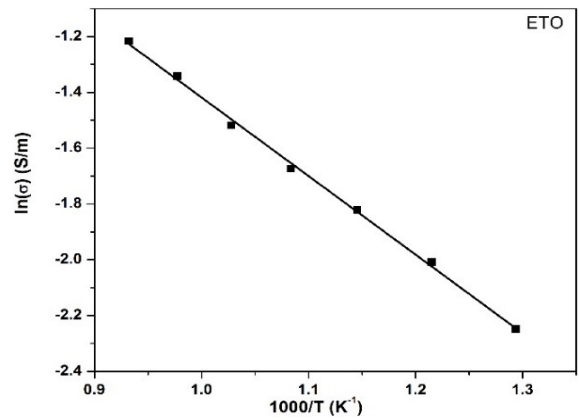
Fig. 5 shows the photoluminescence emission spectra of nanocrystalline ETO. The luminescence is a visible emission with broad spectral lines at 416, 436 nm for ETO. The complete emission lines of the sample with corresponding elements producing emissions are identified with the data book of R. Payling and P. Larkins and are given in Table 1 [30]. The origin of the luminescence may be related to oxygen vacancies or impurities or from the self-trapped excitons, which cause loss of exciton energy through lattice relaxation [31]. In the emission spectra, each wavelength represents a different type of electronic transition caused by a specific structural arrangement. The defects and disorders in the powder may cause a wide band of photoluminescence emission in the visible spectra of light [32]. The results indicate that nanocrystalline ETO is a promising candidate for photoluminescence applications.

The frequency dependent AC conductivity (σ) were calculated from the observed conductance (G) of the sample, measured with the LCR meter, at various temperatures and frequencies using the equation:

$$\sigma = \frac{Gl}{A}, \quad (3)$$

where l is the thickness of the pellet, and A is cross-sectional area of the pellet. The variation of conductivity with temperature at different frequencies is plotted in Fig. 6. It is clear from the figure that the conductivity increases with increasing the frequency and temperature. The trend of a frequency independent conductivity shown by the sample at low frequencies is caused by the random diffusion of charge carriers via hopping. At higher frequencies, σ exhibits dispersion, increasing exponentially and finally becoming almost linear [33]. The conductivity plots of the sample also show prominent transition after 600 °C. These transitions can be associated with the higher oxygen vacancy content in the sample at high temperatures [34]. The conductivities obtained previously for the pyrochlore structured $Er_2Ti_2O_7$ at 1000 °C is $1.3 \cdot 10^{-2} \text{ S}\cdot\text{cm}^{-1}$ [35]. For the present study, the obtained conductivity is $1.04 \cdot 10^{-2} \text{ S/m}$ at 750 °C and 1 MHz. The enhancement of AC conductivity of the material at higher frequencies may be due to reduction in barrier properties of the material with rise in temperature [36].

Activation energies of the conductivity follow the Arrhenius behavior given by the relation:


Fig. 6.

Fig. 7.

$$\sigma = \sigma_0 \exp(-E_a/KT), \quad (4)$$

where σ_0 is a pre-exponential factor that gives the effective number of oxide mobile ions, E_a represents the activation energy, K is the Boltzmann constant, and T represents the absolute temperature. The activation energy values of the samples obtained from the Arrhenius plot in Fig. 7 is 0.24 eV. The result is close to the activation energy value of ionic conductivity in oxygen containing conductors. This proposes that conduction in the compound is mainly related with the oxygen ion mechanism [35].

The impedance spectroscopy is the most consistent method to determine the electrical properties of the materials like bulk, grain boundary, and electrode process. When the dielectric is polarized due to the application of an electric field, it may undergo hopping between sites arranged in three-dimensional arrays, this hopping charges can contribute to the conductivity. The impedance diagram can represent this kind of hopping effect in the dielectrics. The complex impedance plots of ETO within the temperature range 400 up to 850 °C are shown in Fig. 8. In the two semicircular arcs on the complex plane plot, the completed arcs representing the combined contributions of grain and grain boundary effect, and the incomplete arcs show the electrode polarization. In the sample, due to the increase of relaxation frequency of grain polarization, the semicircles of grain conduction changes into an inclined spike at high temperatures. But at the same time, the arc related with the electrode polarization increases at high temperatures due to the increase in the relaxation frequency of electrode polarization [37].

The complex impedance spectrum can be interpreted by means of an appropriate equivalent circuit of parallel resistance – constant phase element for the prepared sample. It simulates the non-ideal capacitive behavior for a depressed semi-circle that deviates from the ideal Debye relaxation [38]. This non-ideal behavior may be caused by the difference in grain orientation, grain boundary and defects in the structure. The experimental data is fitted using the Z-View software and the circuit parameters obtained with the best fit of data is tabulated in Table 2.

Z-View software gives the values of grain resistance (R_g), grain boundary resistance (R_{gb}), constant phase element for grain (Q_g) and for grain boundary (Q_{gb}) of the fitted spectra within 2-3% of the experimental error. Q_g and Q_{gb} values are used to calculate the capacitance of grain and grain boundary by using the relation with a parameter ‘ n ’ that represents deviation of capacitance from ideal behavior [39]

$$C = R^{(1-n)/n} Q^{1/n} \quad (5)$$

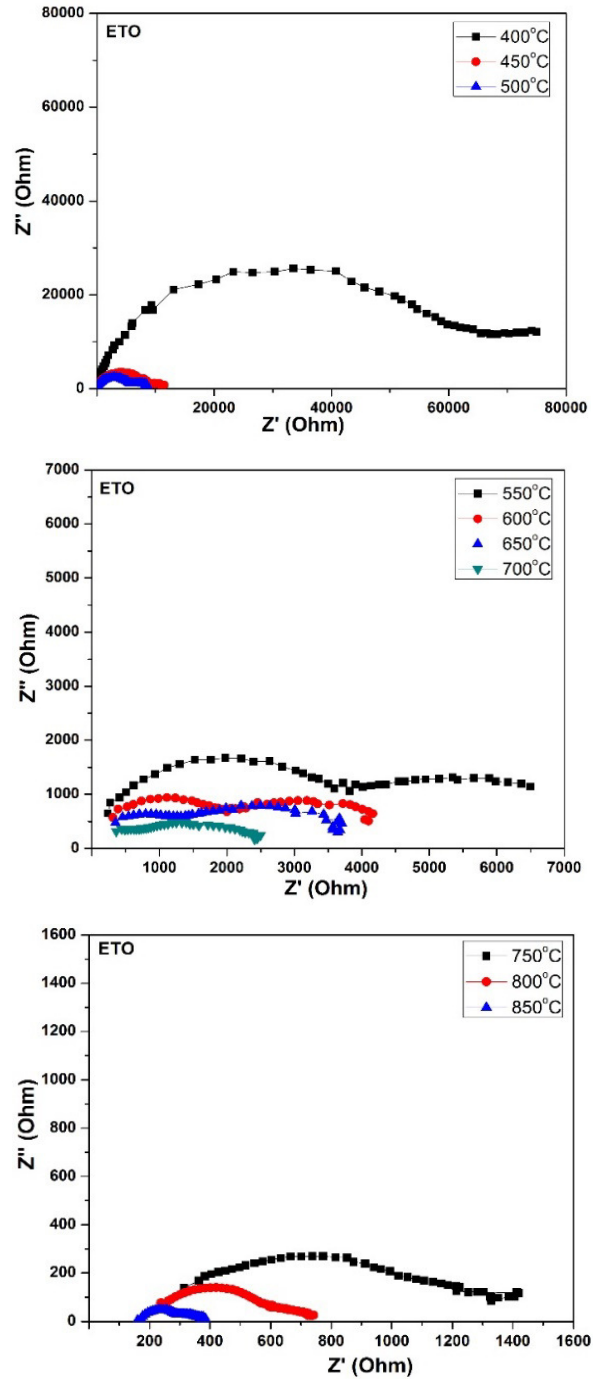


Fig. 8.

Table 2. Resistance (R_g , R_{gb}), capacitance (C_g , C_{gb}) and relaxation time (τ_g , τ_{gb}) of grain and grain boundary of ETO.

T (°C)	R_g (Ω)	R_{gb} (Ω)	n_g	n_{gb}	$C_g(F) \cdot 10^{-11}$	$C_{gb}(F) \cdot 10^{-9}$	$\tau_g(s) \cdot 10^{-7}$	$\tau_{gb}(s) \cdot 10^{-6}$
450	5567	2295	0.938	0.899	12.368	2.158	6.885	4.953
500	4303	1490	0.999	0.879	6.051	1.108	2.604	1.652
550	2484	1349	0.959	0.961	4.086	0.370	1.015	0.499
600	1419	1061	0.924	0.991	3.653	0.194	0.518	0.206

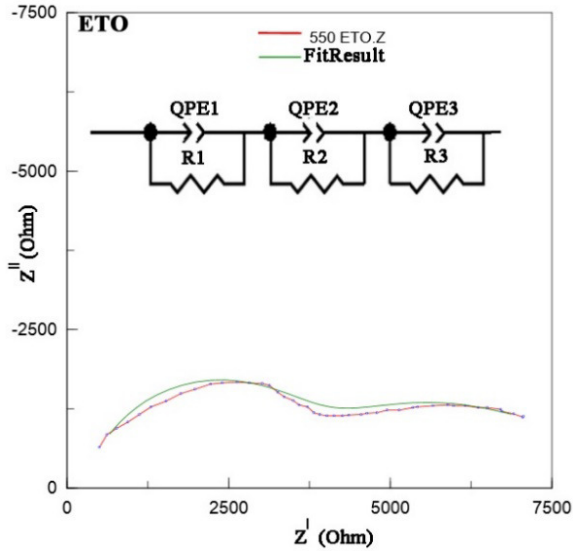


Fig. 9.

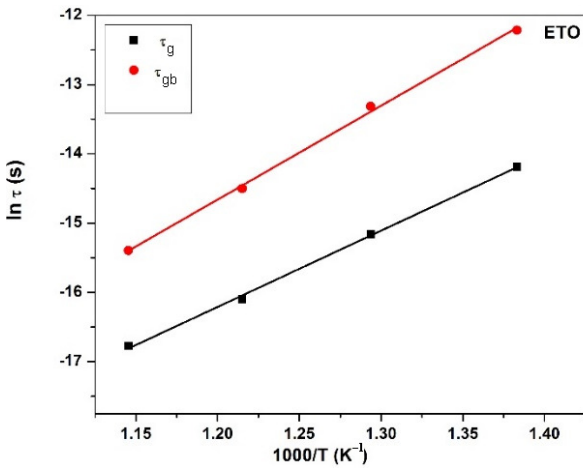


Fig. 10.

The best fit for ETO in a representative temperature with corresponding equivalent circuit is shown in Fig. 9. The grain and grain boundary relaxation times τ_g , τ_{gb} were calculated using the equation:

$$\tau = RC \quad (6)$$

The values of τ_g and τ_{gb} were plotted against the inverse of temperature to yield Arrhenius plot of bulk and grain-boundary relaxation, as shown in Fig. 10.

The grain and grain boundary activation energies of ETO are 0.95 and 1.17 eV, respectively. These values of activation energies are close to those found in the literature for ionic conductors [40, 41]. The difference in the activation energies for conduction and relaxation processes shows that relaxation involves only the hopping energy of the carriers between the localized states, whereas the conduction mechanism involves hopping energy as well as disorder and binding energy of

polarons [42, 43]. This result suggests that the same type of charge carriers are responsible for the conduction and relaxation processes. The straight line graphs in the Arrhenius plot also support this assumption.

4. Conclusion

The nanocrystalline ETO has been prepared using the modified combustion technique. X-ray diffraction analysis exhibits the cubic crystal structure of the compound at room temperature. Raman and FT-IR spectroscopic studies confirm the cubic pyrochlore structure. UV-Vis diffuse reflectance spectroscopy provides the band gap energy values of the material. The photoluminescence spectra of the sample show strong emission within the visible range of spectrum. The electrical conductivity of the sample as a function of temperature shows linear behavior over the entire temperature range. Impedance plane plots obtained within the frequency range 100 Hz to 5 MHz show mainly the bulk and grain boundary phases. The decrease in grain and grain boundary resistances with temperature suggests a thermally activated conduction mechanism. Thermal activation has been found to be of hopping type, and the mobility of charge carriers increases with increasing temperature. The activation energies of grain and grain boundary as well as the electrical conductivity values prove application of these materials for fabrication of electrolytes in solid oxide fuel cells.

Acknowledgements

The authors acknowledge the Kerala State Council for Science, Technology and Environment, Government of Kerala for financial assistance.

References

1. Jingbao Lian, Jiao He, Xue Zhang, Feng Liu, Fractional precipitation synthesis and photoluminescence of $\text{La}_2\text{Ti}_2\text{O}_7:\text{xEu}^{3+}$ phosphors. *Solid State Sci.* 2016. **61**. P. 9–15. <https://doi.org/10.1016/j.solidstatesciences.2016.06.012>.
2. Malkin B.Z., Zakirov A.R., Popova M.N. *et al.* Optical spectroscopy of $\text{Yb}_2\text{Ti}_2\text{O}_7$ and $\text{Y}_2\text{Ti}_2\text{O}_7:\text{Yb}^{3+}$ and crystal-field parameters in rare-earth titanate pyrochlores. *Phys. Rev. B.* 2004. **70**. P. 075112. <https://doi.org/10.1103/PhysRevB.70.075112>.
3. Hatnean M.C., Lees M.R., Balakrishnan G. Growth of single-crystals of rare-earth zirconate pyrochlores, $\text{Ln}_2\text{Zr}_2\text{O}_7$ (with Ln = La, Nd, Sm, and Gd) by the floating zone technique. *J. Cryst. Growth.* 2015. **418**. P. 1–6. <https://doi.org/10.1016/j.jcrysgro.2015.01.037>.
4. Jafar M., Achary S.N., and Tyagi A.K. Phase evolution studies in $\text{CaZrTi}_2\text{O}_7\text{-RE } 2\text{Ti}_2\text{O}_7$ (RE = Nd^{3+} , Sm^{3+}) system: Futuristic ceramic host matrices for nuclear waste immobilization. *AIP Conf. Proc.* 2014. **1591**. P. 55–57.

5. Joseph L.K., Dayas K.R., Damodar S., Krishnan B., Krishnankutty K., Nampoori V.P.N., and Radhakrishnan P. Photoluminescence studies on rare earth titanates prepared by self-propagating high temperature synthesis method. *Spectrochim. Acta – Part A Mol. Biomol. Spectrosc.* 2008. **71**, no. 4. P. 1281–1285. <https://doi.org/10.1016/j.saa.2008.03.030>.
6. Singh B.P., Parchur A.K., Singh R.K., Ansari A.A., Singh P., and Rai S.B. Structural and up-conversion properties of Er^{3+} and Yb^{3+} co-doped $\text{Y}_2\text{Ti}_2\text{O}_7$ phosphors. *Phys. Chem. Chem. Phys.* 2013. **15**, no. 10. P. 3480–3489. <https://doi.org/10.1039/C2CP44195K>.
7. Kreuer K.D., Adams S., Münch W., Fuchs A., Klock U., and Maier J. Proton conducting alkaline earth zirconates and titanates for high drain electrochemical applications. *Solid State Ionics.* 2001. **145**, no. 1–4. P. 295–306. [https://doi.org/10.1016/S0167-2738\(01\)00953-5](https://doi.org/10.1016/S0167-2738(01)00953-5).
8. Sohn J.M. and Woo S.I. The effect of chelating agent on the catalytic and structural properties of $\text{Sm}_2\text{Zr}_2\text{O}_7$ as a methane combustion catalyst. *Catal. Lett.* 2002. **79**, no. 1. P. 45–48.
9. Jafar M., Sengupta P., Achary S.N., and Tyagi A.K. Phase evolution and microstructural studies in $\text{CaZrTi}_2\text{O}_7$ (zirconolite)- $\text{Sm}_2\text{Ti}_2\text{O}_7$ (pyrochlore) system. *J. Eur. Ceram. Soc.* 2014. **34**, no. 16. P. 4373–4381. <https://doi.org/10.1016/j.jeurceramsoc.2014.07.001>.
10. Cann D.P., Randall C.A., and ShROUT T.R. Investigation of the dielectric properties of bismuth pyrochlores. *Solid State Commun.* 1996. **100**, no. 7. P. 529–534. [https://doi.org/10.1016/0038-1098\(96\)00012-9](https://doi.org/10.1016/0038-1098(96)00012-9).
11. Vassen R., Cao X., Tietz F., Basu D., and Stöver D. Zirconates as new materials for thermal barrier coatings. *J. Am. Ceram. Soc.* 2004. **83**, no. 8. P. 2023–2028. <https://doi.org/10.1111/j.1151-2916.2000.tb01506.x>.
12. Coles G.S.V., Bond S.E., and Williams G. Metal stannates and their role as potential gas-sensing elements. *J. Mater. Chem.* 1994. **4**, no. 1. P. 23–27. <https://doi.org/10.1039/JM9940400023>.
13. Murphy A.B. Band-gap determination from diffuse reflectance measurements of semiconductor films, and application to photoelectrochemical water-splitting. *Sol. Energy Mater. Sol. Cells.* 2007. **91**, no. 14. P. 1326–1337. <https://doi.org/10.1016/j.solmat.2007.05.005>.
14. Knop O., Brisse F., Castelliz L. Pyrochlores. V. Thermoanalytic, X-ray, neutron, infrared, and dielectric studies of $\text{A}_2\text{Ti}_2\text{O}_7$ titanates. *Can. J. Chem.* 1969. **47**. P. 971–990.
15. Jih Hoon Park, M.-G. Kwak, Choung-Soo Kim *et al.* Synthesis and spectral properties of rare-earth ions-doped nano-sized Y_2O_3 phosphors. *J. Korean Phys. Soc.* 2006. **48**, no. 6. P. 1369–1373.
16. Maczka M., Hanuza J., Hermanowicz K., Fuentes A.F., Matsuhira K., and Hiroi Z. Temperature-dependent Raman scattering studies of the geometrically frustrated pyrochlores $\text{Dy}_2\text{Ti}_2\text{O}_7$, $\text{Gd}_2\text{Ti}_2\text{O}_7$ and $\text{Er}_2\text{Ti}_2\text{O}_7$. *J. Raman Spectrosc.* 2008. **39**, no. 4. P. 537–544. <https://doi.org/10.1002/jrs.1875>.
17. Tyagi A.K., Chavan S.V., and Purohit R.D. Visit to the fascinating world of nano-ceramic powders via solution-combustion. *Indian J. Pure Appl. Phys.* 2006. **44**, no. 2. P. 113–118.
18. Sam Solomon, Aneesh George, J. Thomas, Annamma John. Preparation, characterization, and ionic transport properties of nanoscale $\text{Ln}_2\text{Zr}_2\text{O}_7$ ($\text{Ln} = \text{Ce}, \text{Pr}, \text{Nd}, \text{Sm}, \text{Gd}, \text{Dy}, \text{Er}, \text{and Yb}$) energy materials. *J. Electron. Mater.* 2015. **44**, no. 1. P. 28–37. <https://doi.org/10.1007/s11664-014-3473-y>.
19. Subramanian M.A., Aravamudan G., and Subba Rao G.V. Oxide pyrochlores – A review. *Prog. Solid State Chem.* 1983. **15**, no. 2. P. 55–143. [https://doi.org/10.1016/0079-6786\(83\)90001-8](https://doi.org/10.1016/0079-6786(83)90001-8).
20. Garbout A., Ben Taazayet-Belgacem I., and Férid M. Structural, FT-IR, XRD and Raman scattering of new rare-earth-titanate pyrochlore-type oxides $\text{LnEuTi}_2\text{O}_7$ ($\text{Ln} = \text{Gd}, \text{Dy}$). *J. Alloys Compd.* 2013. **573**. P. 43–52. <https://doi.org/10.1016/j.jallcom.2013.03.279>.
21. Busca G., Ramis G., Gallardo-Amores J.M., Escribano V.S., and Piaggio P. FT Raman and FTIR studies of titanias and metatitanate powders. *J. Chem. Soc. Faraday Trans.* 1994. **90**, no. 20. P. 3181–3190. <https://doi.org/10.1039/ft9949003181>.
22. Saha S., Prusty S., Singh S., Suryanarayanan R., Revcolevschi A., and Sood A.K. Tuning of phonon anharmonicity in pyrochlore titanates: Temperature-dependent Raman studies of $\text{Sm}_2\text{Ti}_{2-x}\text{Zr}_x\text{O}_7$ ($x = 0, 1/2, 3/4, \text{and } 2$) and stuffed spin-ice $\text{Ho}_{2+x}\text{Ti}_{2-x}\text{O}_{7-x/2}$ ($x = 0, 1/3, \text{and } 2/3$). *J. Raman Spectrosc.* 2012. **43**, no. 4. P. 549–555. <https://doi.org/10.1002/jrs.3058>.
23. Sonu Kumar and Hem Gupta. First principles study of zone centre phonons in rare-earth pyrochlore titanates, $\text{RE}_2\text{Ti}_2\text{O}_7$ ($\text{RE} = \text{Gd}, \text{Dy}, \text{Ho}, \text{Er}, \text{Lu}; \text{Y}$). *Vib. Spectrosc.* 2012. **62**. P. 180–187.
24. Saha S., Singh S., Dkhil B., Dhar S., Suryanarayanan R., Dhahenne G., Revcolevschi A., and Sood A.K. Temperature-dependent Raman and x-ray studies of the spin-ice pyrochlore $\text{Dy}_2\text{Ti}_2\text{O}_7$ and nonmagnetic pyrochlore $\text{Lu}_2\text{Ti}_2\text{O}_7$. *Phys. Rev. B.* 2008. **78**, no. 21. P. 214102. <https://doi.org/10.1103/PhysRevB.78.214102>.
25. Tauc J. and Menth A. States in the gap. *J. Non. Cryst. Solids.* 1972. **8–10**. P. 569–585. [https://doi.org/10.1016/0022-3093\(72\)90194-9](https://doi.org/10.1016/0022-3093(72)90194-9).
26. Aneesh George, Jijimon K. Thomas, Annamma John, Sam Solomon. Synthesis and characterization of nanocrystalline $\text{A}_6\text{Sb}_4\text{ZrO}_{18}$ ($\text{A} = \text{Ca}, \text{Sr} \text{ and } \text{Ba}$) functional ceramics. *Solid State Ionics.* 2015. **278**. P. 245–253. <https://doi.org/10.1016/j.ssi.2015.07.003>.
27. Barton D.G., Shtein M., Wilson R.D., Soled S.L., and Iglesia E. Structure and electronic properties of solid acids based on tungsten oxide nanostructures. *J. Phys. Chem. B.* 1999. **103**, no. 510. P. 630–640. <https://doi.org/10.1021/jp983555d>.

28. Choudhury B., Dey M., and Choudhury A. Defect generation, d-d transition, and band gap reduction in Cu-doped TiO₂ nanoparticles. *Int. Nano Lett.* 2013. **3**, no. 1. P. 25. <https://doi.org/10.1186/2228-5326-3-25>.
29. López R. and Gómez R. Band-gap energy estimation from diffuse reflectance measurements on sol-gel and commercial TiO₂: A comparative study. *J. Sol-Gel Sci. Technol.* 2012. **61**, no. 1. P. 1–7.
30. Payling R. and Larkins P. *Optical Emission Lines of the Elements*. Wiley, New York, 2000.
31. Tang H., Prasad K., Sanjinès R., Schmid P.E., and Lévy F. Electrical and optical properties of TiO₂ anatase thin films. *J. Appl. Phys.* 1994. **75**, no. 4. P. 2042–2047. <https://doi.org/10.1063/1.356306>.
32. Longo V.M., De Figueiredo A.T., Campos A.B. et al. Different origins of green-light photoluminescence emission in structurally ordered and disordered powders of calcium molybdate. *J. Phys. Chem. A*. 2008. **112**, no. 38. P. 8920–8928. <https://doi.org/10.1021/jp801587w>.
33. Mahato D.K., Dutta A., and Sinha T.P. Dielectric relaxation and ac conductivity of double perovskite oxide Ho₂ZnZrO₆. *Phys. B: Condens. Matter*. 2011. **406**, no. 13. P. 2703–2708. <https://doi.org/10.1016/j.physb.2011.04.012>.
34. Gill J.K., Pandey O.P., and Singh K. Ionic conductivity, structural and thermal properties of Ca²⁺ doped Y₂Ti₂O₇ pyrochlores for SOFC. *Int. J. Hydrogen Energy*. 2012. **37**, no. 4. P. 3857–3864. <https://doi.org/10.1016/j.ijhydene.2011.04.216>.
35. Lyashenko L.P., Belov D.A., Shcherbakova L.G. Conductivity of Sm₂TiO₅ and Sm₂Ti₂O₇. *Inorg. Mater.* 2008. **44**, no. 12. P. 1349–1353. <https://doi.org/10.1134/S0020168508120169>.
36. Provenzano V., Boesch L.P., Volterra V. et al. Electrical relaxation in Na₂O·3SiO₂ glass. *J. Am. Ceram. Soc.* 1972. **55**, no. 10. P. 492–496. <https://doi.org/10.1111/j.1151-2916.1972.tb13413.x>.
37. Xiao-Liang Xia, Jia-Hu Ouyang, Zhan-Guo Lia. Electrical properties of gadolinium-europium zirconate ceramics. *J. Am. Ceram. Soc.* 2010. **93**, no. 4. P. 1074–1080. <https://doi.org/10.1111/j.1551-2916.2009.03505.x>.
38. Ross M.J. Note on the parameterization of the constant-phase admittance element. *Solid State Ionics*. 1984. **13**, no. 2. P. 147–149. [https://doi.org/10.1016/0167-2738\(84\)90049-3](https://doi.org/10.1016/0167-2738(84)90049-3).
39. Idrees M., Nadeem M., and Hassan M.M. Investigation of conduction and relaxation phenomena in LaFe_{0.9}Ni_{0.1}O₃ by impedance spectroscopy. *J. Phys. D: Appl. Phys.* 2010. **43**, no. 15. P. 155401. <https://doi.org/10.1088/0022-3727/43/15/155401>.
40. van Dijk M.P., de Vries K.J., and Burggraaf A.J. Oxygen ion and mixed conductivity in compounds with the fluorite and pyrochlore structure. *Solid State Ionics*. 1983. **9–10**. P. 913–919. [https://doi.org/10.1016/0167-2738\(83\)90110-8](https://doi.org/10.1016/0167-2738(83)90110-8).
41. Burggraaf A.J., van Dijk T., and Verkerk M.J. Structure and conductivity of pyrochlore and fluorite type solid solutions. *Solid State Ionics*. 1981. **5**. P. 519–522. [https://doi.org/10.1016/0167-2738\(81\)90306-4](https://doi.org/10.1016/0167-2738(81)90306-4).
42. Komine S. and Iguchi E. Dielectric properties in LaFe_{0.5}Ga_{0.5}O₃. *J. Phys. Chem. Solids*. 2007. **68**, no. 8. P. 1504–1507. <https://doi.org/10.1016/j.jpcs.2007.03.024>.
43. Eisuke Iguchi and Woo Hwan Jung, Electrical transports of LaFe_{1-x}Ti_xO₃ (x ≤ 0.10). *J. Phys. Soc. Jpn.* 1994. **63**, no. 8. P. 3078–3086. <https://doi.org/10.1143/JPSJ.63.3078>.

Author and CV



Kuttan Pillai Sandeep obtained his Ph.D in 2019 from the University of Kerala, India. He is the author of more than 10 publications. The area of his scientific interests includes nano-ceramics, solid oxide fuel cells and high-*k* gate dielectrics.